

RESEARCH ARTICLE

Computational Observations of the Tip Loss Mechanism Experienced by Horizontal Axis Rotors

A. Wimshurst and R. H. J. Willden

Department of Engineering Science, University of Oxford, Parks Road, Oxford, OX1 3PJ, UK.

ABSTRACT

Blade resolved computations of two different horizontal axis rotors are carried out to investigate the tip loss mechanism experienced by horizontal axis rotors. The tip loss mechanism specifically refers to the effect of the vorticity that is shed from the outboard blade sections, which results in the blade loading dropping off as the tip is approached. In this paper, the shed vorticity is shown to induce a downwash at the rotor plane and spanwise flow accelerations along the blade surfaces. While the downwash reduces the angle of attack of the approach flow, the spanwise flow accelerations lead to additional momentum transport along the blade. This spanwise momentum transport reduces the magnitude and changes the distribution of the static pressure developed on the pressure and suction surfaces of the outboard blade sections. As a result of this modification, the torque producing force drops off faster than the thrust producing force as the tip is approached, resulting in a rotation of the net force vector towards the streamwise direction. This anisotropy must be accounted for by tip flow corrections if the loading on the outboard blade sections is to be computed with sufficient accuracy. In addition, it is also shown that changes in the static pressure distribution cannot be accurately approximated by only modifying the angle of attack of the approach flow, as this would lead to blade loading changes which are inconsistent with the observed behaviour of the lift and drag coefficients on the outboard blade sections. Copyright © 2017 John Wiley & Sons, Ltd.

KEYWORDS

Tip Loss, Tip Correction, Tip Vortex, Spanwise Flow, Rotor aerodynamics, MEXICO

Correspondence

Department of Engineering Science, University of Oxford, Parks Road, Oxford, OX1 3PJ, UK

E-mail: Aidan.Wimshurst@eng.ox.ac.uk

Received . . .

1. INTRODUCTION

At the tip of a rotor blade, the static pressure difference between the pressure and suction surfaces drives flow around the tip of the blade, from the pressure surface to the suction surface. This rotational flow component is convected downstream into the wake as shed vorticity. The shed vorticity induces a downwash at the rotor plane, which reduces the angle of attack on the outboard blade sections. In addition, the shed vorticity also induces spanwise flow accelerations on the outboard regions of the blade (outboard on the pressure surface and inboard on the suction surface). These spanwise flow accelerations transport momentum along the blade and around the tip, reducing the static pressure developed on the pressure surface and increasing the static pressure developed on the suction surface. With a reduced angle of attack (from the induced downwash) and a reduced static pressure difference between the pressure and suction surfaces, the sectional blade loading drops off as the tip of the blade is approached. However, beyond this qualitative understanding, only a limited number of studies have been carried out to investigate rotor tip flow physics in detail.

The majority of tip flow studies have been carried out with the aim of reducing the strength of the tip vortex and making it more diffuse, by re-designing the tip geometry. A more diffuse tip vortex is likely to reduce noise emissions, as long as flow separation is not induced by the increased angle of attack (which arises from the reduction in induced downwash) [1]. Madsen and Fuglsang [2] for example, compared blunt and tapered tip geometries in a series of blade resolved computations. They found that the gradual chord reduction adopted by the tapered tip geometries led to a more

gradual reduction in circulation strength and a more diffuse tip vortex than blunt tip geometries. Ferrer and Munduate [3] carried out a similar investigation and deduced that the induced downwash from the tip vortex was weaker when adopting a tapered tip geometry than a blunt tip geometry. However, they also found that changes to the surface pressure distribution could not be entirely accounted for by a modification to the angle of attack (arising from the induced downwash) alone.

As an alternative to modifying the planform shape of the tip region, some authors have added winglets to the tip of wind turbine blades. Winglets aim to displace the tip vortex away from the blade, reducing the downwash induced at the rotor plane and disrupting the spanwise momentum transport between the pressure and suction surfaces. Johansen and Sørensen [4] for example, compared the changes in blade loading induced by upwind and downwind facing winglets. They found that both upwind and downwind facing winglets improved the induced downwash distribution, leading to greater torque generation. However, the addition of winglets also led to an undesirable increase in rotor thrust.

Rather than propose such modifications to the tip geometry, this paper will instead provide observations of the local flow field and the blade loading distribution in the vicinity of the blade tip. These observations will then be used to explain the blade loading behaviour that has been observed on the outboard sections of several rotors in the literature.

2. TIP FLOW CORRECTIONS

While blade resolved computations can directly account for the induced downwash at the rotor plane and the spanwise flow accelerations along the blade, low order rotor models (such as the blade element momentum (BEM) and actuator line (AL) methods) operate using the flow independence principle and neglect the spanwise flow along the blade. Hence, these methods must be corrected if the blade loading on the outboard sections (and near the root) is to be computed with sufficient accuracy. However, the mechanism that leads to the reduction in blade loading as the tip is approached (particularly from the induced spanwise flow), remains uncertain. As a result of this uncertainty, a variety of different corrections have been proposed in an attempt to force the loading to drop off as the tip is approached. While it is usually assumed that the loading must tend to zero as the tip is approached, a general consensus for how this should be achieved in numerical models has not yet been reached.

Prandtl [5] type corrections (such as the Goldstein [6] and Glauert [7] corrections) are the most widely adopted type of tip flow correction and are required in the BEM method to account for the lack of discrete blade effects in the azimuthal averaging process (see Burton et al. [8] for details of the BEM method). By forcing the axial induction factor to tend to 1 at the tip, the angle of the incident flow vector relative to the rotor plane (ϕ) is forced to zero, which reduces the angle of attack (α) on the outboard blade sections. The reduced angle of attack then reduces the lift and drag coefficients, which causes the blade loading to drop off as the tip is approached. The reduction in angle of attack from the tip flow correction is similar to the reduction in angle of attack that is induced by the downwash from the shed vorticity. However, the Prandtl type corrections were all derived using idealised models of the rotor wake and hence are not precisely correct for real rotors.

Despite the inaccuracies of the Prandtl type correction factors (due to the approximations adopted for the rotor wake), the angle of the incident flow vector relative to the rotor plane (ϕ) at the blade tip is (in general) not zero [9]. Hence, Shen et al. [9] deduced that Prandtl type correction factors (alone) will always be insufficient for correcting the blade loading. To address this deficiency, Shen et al. proposed an additional correction to the blade loading and calibrated it using empirical data from the NREL Phase VI and the Swedish WG 500 rotors. Wimshurst and Willden [10] proposed an improvement to this correction, to better match simulation results. Their modification allowed the torque producing force to drop off faster than the thrust producing force as the tip of the blade is approached, resulting in a significant improvement in accuracy of the tip flow correction. However, despite the improved accuracy that was achieved with the modified tip flow correction (mainly due to empirical calibration), a physical explanation has not yet been proposed to support the new calibration.

In this paper, blade resolved computations will be used to directly observe the reduction in blade loading that occurs as the tip of the blade is approached and provide a physical explanation for the tip loss mechanism.

3. COMPUTATIONAL DETAILS

Two distinctly different rotors are analysed in this work, in order to demonstrate that the same fundamental characteristics of the tip loss mechanism are exhibited by different horizontal axis rotors with substantially different solidities. The first rotor is the 3 bladed 4.5m diameter wind turbine rotor that was used in the Model Experiments in Controlled Conditions (MEXICO) experiments. The chord and twist distributions for this rotor are shown in Fig. 1 and details of the MEXICO experiments can be found in the Mexnext final report [11]. This rotor has a tapered tip geometry (see Boorsma and Schepers [12] for details) and has been analysed in a series of blade resolved computations by several authors including: Bechmann et al. [13], Guntur and Sørensen [14] and Wimshurst and Willden [15]. The aerofoil sections vary along the span, with the DU91-W2-250 from $r/R = 0.2$ to 0.46, the RISØ-A1-21 from $r/R = 0.54$ to 0.66, the NACA 64-418

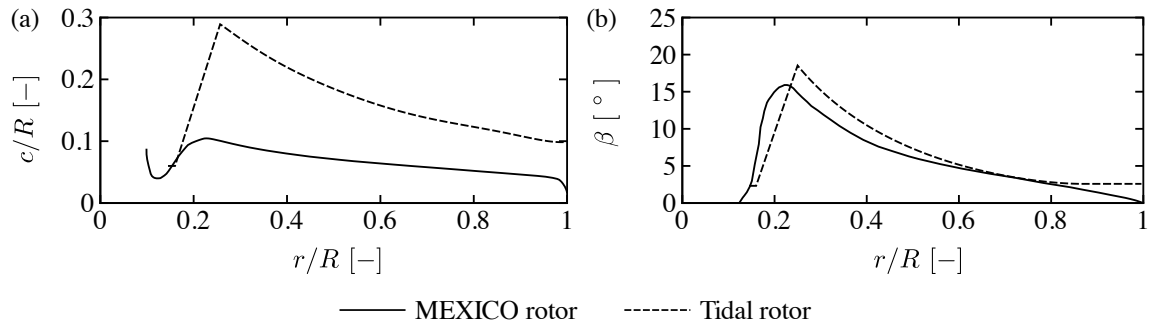


Figure 1. (a) Chord and (b) twist distributions for the MEXICO rotor [18] and the Tidal rotor [17].

from $r/R = 0.74$ to 1.0 and proprietary transition pieces in between. Despite the unknown aerodynamic behaviour of the transition pieces, they are sufficiently far from the tip of the blade that they are not expected to influence the tip flow physics significantly in this investigation.

The second rotor is a 3 bladed, 20m diameter tidal turbine rotor with a blunt tip geometry, which will hereafter be referred to as the Tidal rotor. This rotor uses the RISØ-A1-24 aerofoil along the entire span, except for the region inboard of $r/R = 0.25$, where the aerofoil is blended into a cylinder to facilitate pitching at the root. The rotor was originally designed by Schluntz and Willden [16] and has been analysed in a series of blade resolved computations by Wimshurst and Willden [17]. Fig. 1 shows the chord and twist distributions for this rotor. Although the MEXICO rotor and the Tidal rotor have similar design tip-speed-ratios (6.67 for the MEXICO rotor and 5.0 for the Tidal rotor), the Tidal rotor has a much greater chord length than the MEXICO rotor. This is primarily because the Tidal rotor is specifically designed to operate in a closely packed array of tidal devices, with a tip-to-tip spacing of one diameter between devices. Under these conditions, interaction effects between neighbouring devices are significant and higher thrust may be applied to achieve a higher power coefficient [16]. To meet the greater thrust demands without increasing the design tip-speed-ratio, a higher solidity rotor is required with a greater chord length. For more details of the rotor design process and the effect of blockage on rotor design, the reader is referred to Schluntz and Willden [16]. While the MEXICO rotor and the Tidal rotor have considerably different blade and tip geometries, the same tip loss mechanism will be shown to be present for both rotors.

The computations were carried out in steady uniform flow at the design tip-speed-ratio (6.67 for the MEXICO rotor and 5.0 for the Tidal rotor) and the Multiple Reference Frame (MRF) approach was used to simulate rotor rotation. While flow unsteadiness near the blade root may not be accurately captured by the MRF approach, the focus of this investigation is the outboard region of the blade. As long as the tip flow remains attached (which was found to be the case for all computations carried out in this work), the MRF approach is appropriate to study the tip flow physics. A virtually unblocked cylindrical domain was adopted for both rotors (the rotor swept area occupies 1% of the circular cross-sectional area of the domain), with the inlet placed $5R$ upstream of the rotor plane and the outlet placed $14R$ downstream of the rotor plane.

For both rotors, a block structured mesh was fitted around the blades with a C-C type blocking topology, as shown in Fig. 2. Mesh sensitivity studies were carried out for both rotors, which can be found in Wimshurst and Willden [15] (for the MEXICO rotor) and Wimshurst and Willden [17] (for the Tidal rotor). For both rotors, 58 cells were placed in the chordwise direction along the pressure and suction surfaces (individually). These cells were clustered towards the leading and trailing edges, as shown in Fig. 2 and 3. In the wall normal direction, a wall resolved approach was adopted for the MEXICO rotor ($y^+ < 5$), while a wall function approach was adopted for the Tidal rotor ($30 < y^+ < 200$). The consequences of the wall function modelling were investigated by Wimshurst and Willden [17] and found to only be significant at high angles of attack (low tip-speed-ratios). In this investigation, only the design tip-speed-ratio was considered. Hence, the wall function approach was deemed to be acceptable for the Tidal rotor, as the flow remains attached and at a low angle of attack on the outboard blade sections at the design condition (this will be shown explicitly in Section 5). However, the tip geometry of the MEXICO rotor blade (the outer 5% of the blade) is swept and tapered. For such a blade, a wall resolved approach is essential to capture the complex tip flow, as the flow has been found to separate prematurely on some rotors in the literature that adopt a swept and tapered tip geometry (see Hansen and Johansen [1] for example).

In the spanwise direction, 130 cells were used along the MEXICO rotor blade, while 68 cells were used along the Tidal rotor blade. More cells were required for the MEXICO rotor blade than the Tidal rotor blade, in order to reduce the aspect ratio of the thin boundary layer cells (due to the wall resolved approach). For both rotors, the cells were clustered towards the blade tip (as shown in Fig. 3), with a growth ratio of 1.2 back along the span from the tip. The overall mesh for the MEXICO rotor contained approximately 17.2 million hexahedral cells, while the overall mesh for the Tidal rotor contained approximately 6.3 million hexahedral cells.

The steady Reynolds-averaged Navier-Stokes (RANS) equations were solved using the open source code OpenFOAM (version 2.3.1) with the $k - \omega$ SST model [19] for turbulence closure and the SIMPLE algorithm [20] for pressure-velocity

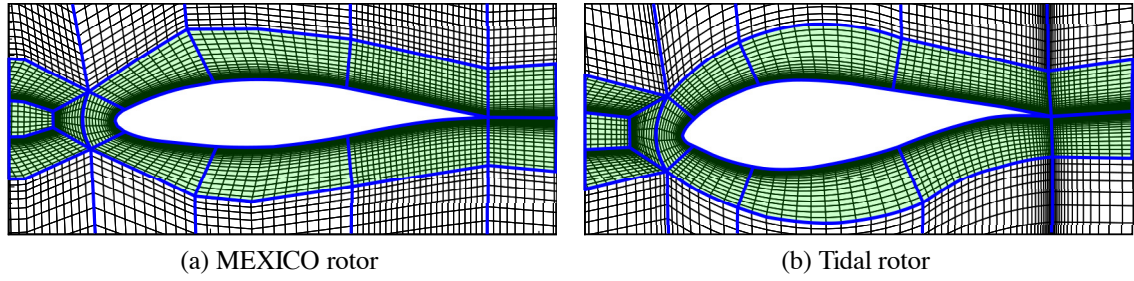


Figure 2. A slice through the (a) MEXICO rotor and (b) Tidal rotor meshes (normal to the blade axis), at $r/R = 0.9$. The blocking edges are highlighted in blue and the C-C blocking topology is shaded in green.

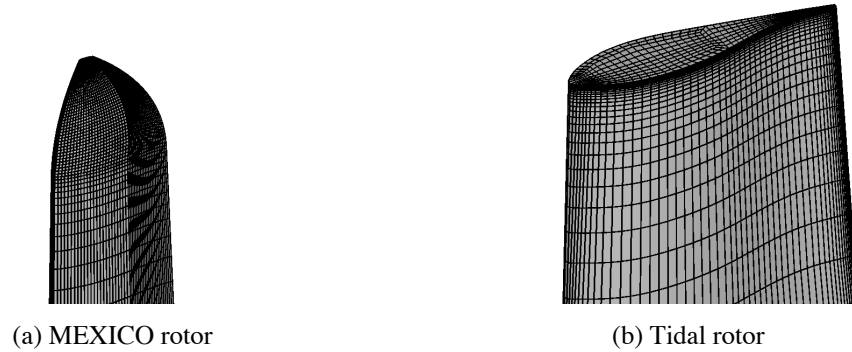


Figure 3. Surface mesh on the outboard regions ($r/R > 0.9$) of (a) the MEXICO rotor blade and (b) the Tidal rotor blade. The blade is viewed from the front and the rotor rotates anti-clockwise.

coupling. Central differencing was used for face interpolation of all the Laplacian and gradient terms, while a flux limited form of central differencing with the Sweby [21] limiter was used for the convection terms. For the MEXICO rotor, the inlet values of k and ω were chosen to replicate the conditions in the Large Low-speed facility of the German-Dutch wind tunnels (where the experiments were carried out) as closely as possible. More specifically, the values of k and ω were computed based on a turbulence intensity of 0.48% and a length scale of 10% of the average blade chord [11]. On the other hand, the inlet values of k and ω for the Tidal rotor were chosen to be representative of the turbulence levels present in real tidal channels (a turbulence intensity of 10% and a length scale of 14m) [22]. At the domain outlet, zero gradient conditions were applied for all flow variables, except for the static pressure, which was assigned a fixed value of 0. On the outer (curved surface) of the cylindrical domain, symmetry conditions were applied for all flow variables.

4. TIP LOSS MECHANISM

Moving outboard from the root section of a rotor blade towards the tip, the static pressure difference between the pressure and suction surfaces generally increases (assuming only modest blade taper), due to the increased dynamic pressure that is incident on the blade. This might imply that the greatest static pressure difference (and hence the maximum blade loading) occurs at the very tip of the blade. However, at the very tip of the blade, the static pressure must equalise between the pressure and suction surfaces. As a result, an additional static pressure gradient is generated in the spanwise direction on the outboard blade sections. This static pressure gradient causes the static pressure to increase on the suction surface as the tip of the blade is approached (an adverse pressure gradient) and decrease on the pressure surface as the tip of the blade is approached (a favourable pressure gradient). Hence, the maximum static pressure difference between the pressure and suction surfaces actually occurs slightly inboard from the tip of the blade and the blade loading drops off as the tip is approached.

These static pressure changes can be observed qualitatively in Fig. 4, which shows contours of static pressure coefficient (C_{pre}) on the pressure and suction surfaces of the MEXICO rotor blade and the Tidal rotor blade. In Fig. 4, the static pressure coefficient has been defined as,

$$C_{pre} = \frac{p - p_{\infty}}{\frac{1}{2}\rho[U_{\infty}^2 + (\Omega r)^2]} \quad (1)$$

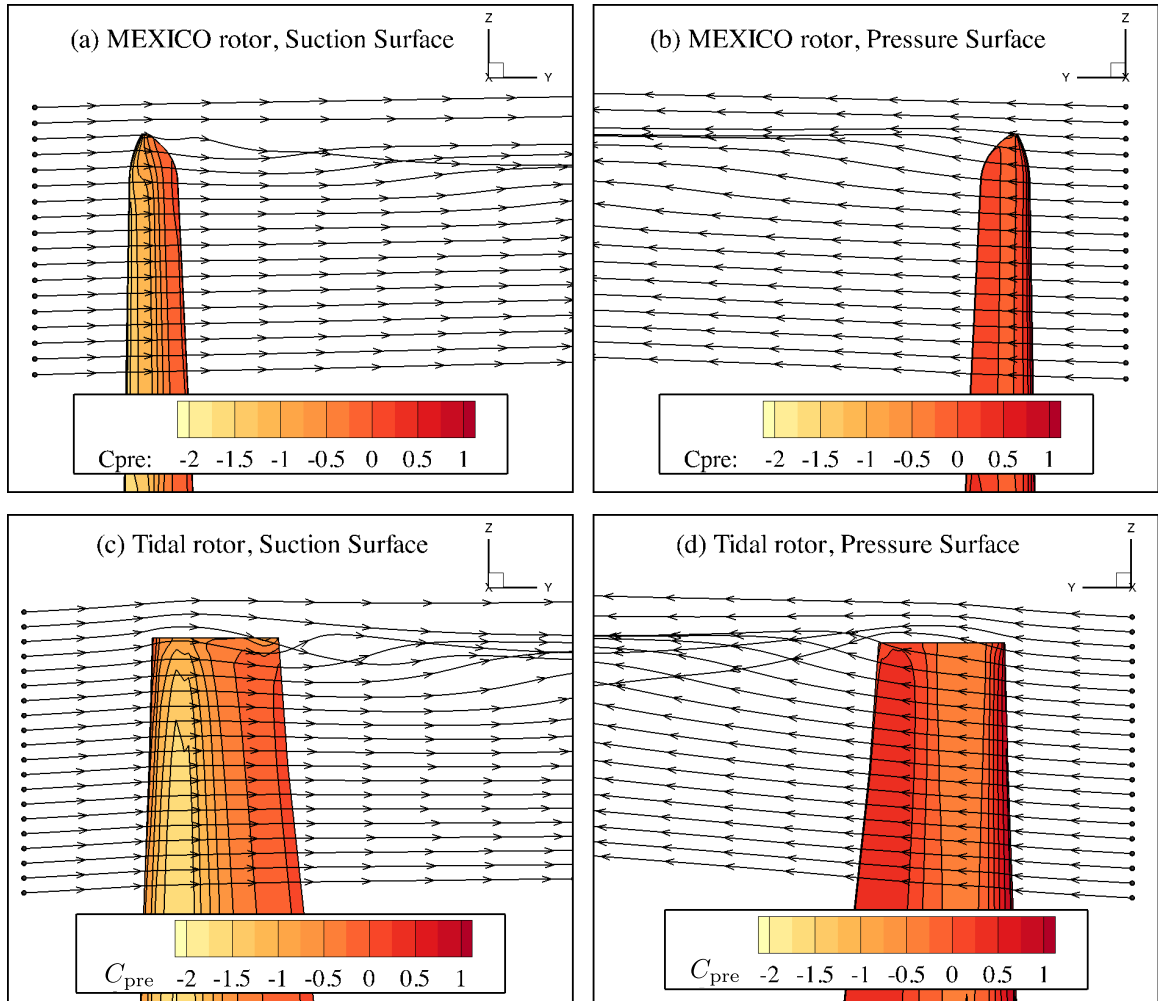


Figure 4. Contours of static pressure coefficient (C_{pre}) on the outboard sections of the MEXICO rotor (a and b) and the Tidal rotor (c and d). The streamlines were released $R/10$ upstream of the blade.

where p is the static pressure, p_∞ is the freestream static pressure, ρ is the fluid density, U_∞ is the freestream velocity and Ω is the rotational speed of the rotor. The approximate dynamic pressure incident on the aerofoil sections has been used for this normalisation (rather than a dynamic pressure based on the relative velocity magnitude) because it is generally not possible to extract consistent values for the axial and swirl induction factors local to the blade section from the computed velocity field, as they vary with the location where the velocity field is sampled.

As shown in Fig. 4, the favourable pressure gradient on the pressure surface causes the incident flow to accelerate in the spanwise direction (defining positive spanwise flow acceleration as increasing spanwise flow velocity towards the tip), driving the flow outboard and bending the streamlines towards the tip. Conversely, the adverse pressure gradient on the suction surface causes the incident flow to decelerate in the spanwise direction (the spanwise flow velocity decreases as the tip is approached), driving the flow inboard and bending the streamlines away from the tip. Hence, a rotational flow component is generated around the tip of the blade, driving the fluid outboard on the pressure surface, around the tip and inboard on the suction surface. This rotational flow component is convected downstream of the blade into the wake as shed vorticity.

Conceptually, the shed vorticity has two main effects on the local flow field around the rotor blade. These effects are shown schematically in Fig. 5. Firstly, the shed vorticity induces a downwash at the rotor plane, which reduces the angle of attack on the outboard blade sections. The reduced angle of attack then reduces the sectional lift and drag coefficients developed by the outboard blade sections, by modifying the static pressure distribution. However, the induced downwash (and the resultant change in angle of attack) is not straightforward to extract directly from the computed velocity field. This is because it is difficult to compute consistent values for the axial and swirl induction factors local to the blade section, as

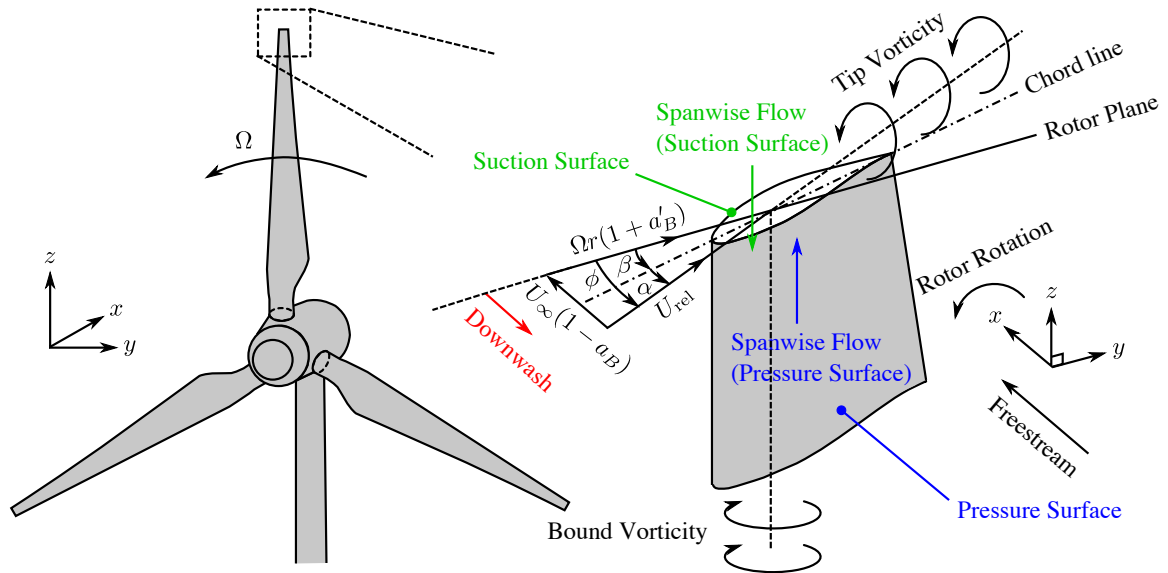


Figure 5. Schematic diagram of the effect of the shed vorticity on the outboard blade sections. The induced downwash is highlighted in red, the spanwise flow on the pressure surface is highlighted in blue and the spanwise flow on the suction surface is highlighted in green.

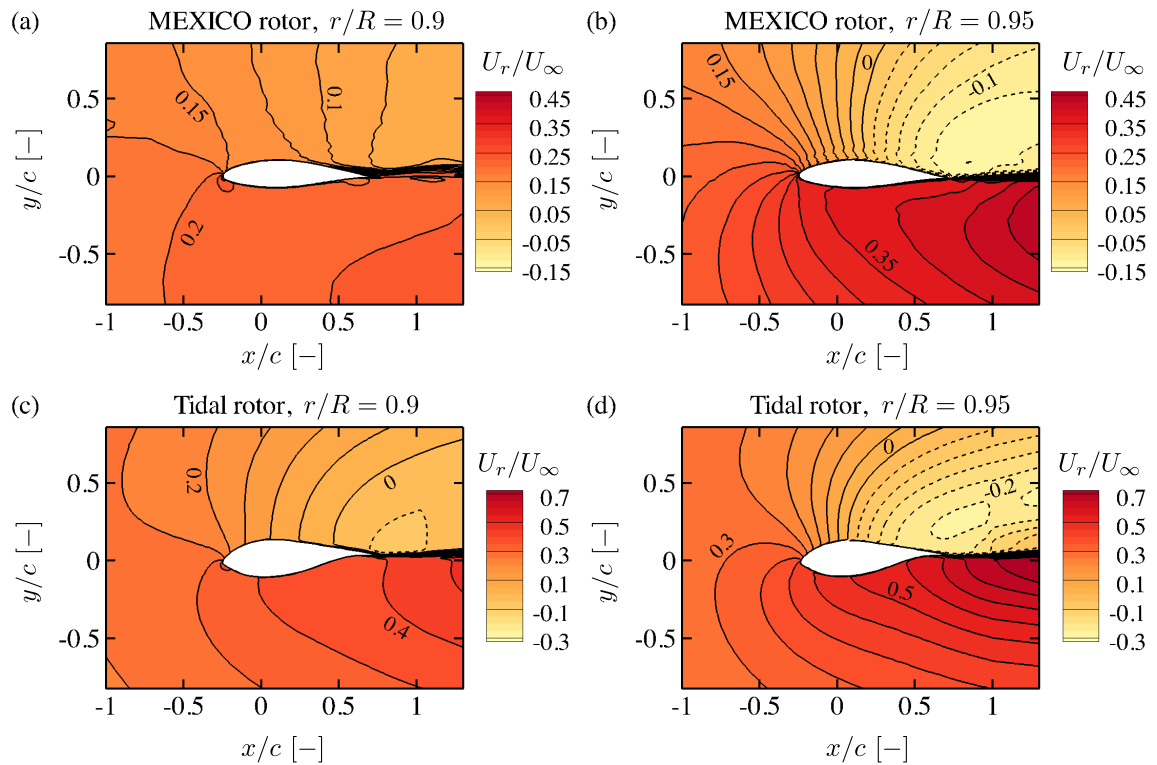


Figure 6. Contours of spanwise velocity (U_r) on slices through the MEXICO rotor blade and the Tidal rotor blades at $r/R = 0.9$ (a and c) and $r/R = 0.95$ (b and d). Positive contours are shown with solid lines, while negative contours are shown with dashed lines.

they vary with the location where the velocity field is sampled. Hence, the induced downwash will be identified indirectly in section 5 instead, by observing the changes in the static pressure distribution on the blade surface.

The second effect of the shed vorticity is the spanwise flow accelerations that are induced on the outboard blade sections. Unlike the induced downwash, these spanwise flow accelerations can be identified directly from the local velocity field. Fig. 6 shows contours of the spanwise velocity component (U_r) on two slices through the computational domain (normal to

the blade axis) at $r/R = 0.9$ and $r/R = 0.95$. In general, the spanwise flow that is induced on the outboard blade sections is outboard on the pressure surface and inboard on the suction surface (as positive U_r indicates outboard flow and negative U_r indicates inboard flow). The direction of the accelerations is consistent with the observed static pressure coefficient changes and also the rotation direction of the shed vorticity (outboard on the pressure surface, around the tip and inboard on the suction surface).

Fig. 6 also shows that the strength of the spanwise flow varies along the aerofoil chord. Starting at the leading edge, the spanwise velocity is continuous between the pressure and suction surfaces. Hence, the difference in the spanwise velocity between the pressure and suction surfaces is small and little vorticity is generated. Moving in the chordwise direction towards the trailing edge, the strength of the spanwise velocity increases, with the flow being driven increasingly outboard on the pressure surface and increasingly inboard on the suction surface. Therefore, the difference in spanwise velocity between the pressure and suction surfaces increases in the chordwise direction, resulting in a build up of vorticity, which is eventually shed from the blade at the trailing edge.

The spanwise flow accelerations that are induced by the shed vorticity are balanced (through spanwise momentum conservation) by the spanwise pressure gradients that are developed on the outboard blade sections. With a reduced static pressure difference between the pressure and suction surfaces, the blade loading drops off as the tip is approached. However, the manner in which the loading drops off is dependent on the blade geometry and therefore varies between rotors. This drop off in the blade loading is critical for developing accurate tip flow corrections. Hence, the manner in which the blade loading drops off will be examined in more detail in the next section.

5. SURFACE PRESSURE CHANGES

In order to examine the changes in blade loading that occur when moving outboard towards the tip of the blade, Fig. 7 shows the static pressure coefficient distribution on three slices through the MEXICO rotor blade (normal to the blade axis) at $r/R = 0.9$, 0.95 and 0.98 . Since it is not possible to accurately determine the angle of attack and relative velocity magnitude incident on the blade sections (due to the unknown axial and swirl induction factors local to the blade sections), the static pressure coefficient distribution for the 2D NACA 64-418 aerofoil is shown for comparison over a range of angles of attack instead. With this approach, the combined effect of induced downwash (reducing the angle of attack) and spanwise flow accelerations on the outboard blade sections can be observed indirectly, despite not being able to exactly quantify the angle of attack experienced by the 3D rotor blade. For the 2D NACA 64-418 aerofoil, the computations were carried out using a mesh structure that closely resembles the mesh structure on a slice through the 3D rotor blade (normal to the blade axis) at $r/R = 0.9$, and the resulting static pressure coefficient is defined using equation 1 with $\Omega = 0$.

At $r/R = 0.9$, the static pressure coefficient distribution near the leading edge of the pressure and suction surfaces ($x/c < 0.4$) shows close agreement with the 2D static pressure distribution at an angle of attack of somewhere between 6° and 7° . Moving along the chord away from the leading edge ($x/c > 0.4$), the static pressure increases on the suction surface. By $x/c = 0.7$, the suction developed is even weaker than the suction developed by the 2D NACA 64-418 aerofoil at an angle of attack of 0° . This reduction in suction is generated by the inboard transport of momentum from the shed vorticity, which can be seen in Fig. 4. The inboard transport of momentum decelerates the velocity magnitude, which increases the static pressure on the suction surface. Conversely, on the pressure surface the static pressure starts to decrease slightly towards the trailing edge. This reduction in static pressure is generated by the outboard transport of momentum (or outboard acceleration) due to the shed vorticity, which can also be seen in Fig. 4.

Moving outboard to $r/R = 0.95$, the differences in static pressure coefficient between the 3D rotor blade and the 2D aerofoil are magnified. Near the leading edge of the suction surface, the static pressure coefficient distribution for the 3D rotor blade now approximately follows the static pressure coefficient distribution of the 2D NACA 64-418 aerofoil at an angle of attack of somewhere between 5° and 6° . Additionally, the static pressure distribution near the leading edge of the pressure surface now more closely follows the static pressure distribution of the 2D NACA 64-418 aerofoil at an angle of attack of 6° . Between $r/R = 0.9$ and 0.95 , the (leading edge based) angle of attack therefore appears to reduce by around 1° . As the twist angle of the rotor blade reduces by around 0.5° between these locations, the angle of the incident flow vector to the rotor plane reduces by around 1.5° between $r/R = 0.9$ and 0.95 . This reduction in the angle of the incident flow vector can be attributed to the increased downwash from the shed vorticity, as the strength of the induction from the shed vorticity increases as the tip is approached.

In addition, the strength of the spanwise flow accelerations (that are induced by the shed vorticity) increase when moving outboard from $r/R = 0.9$ to $r/R = 0.95$, due to the proximity of the tip vortex. Hence, the static pressure distribution departs even more significantly from the 2D static pressure distribution at $r/R = 0.95$ than at $r/R = 0.9$. Fig. 7 shows that at $r/R = 0.95$, the static pressure distribution on the pressure and suction surfaces does not completely follow any of the 2D static pressure distributions, at any angle of attack. It follows that an angle of attack correction (alone) will always be insufficient to capture the static pressure changes induced by the shed vorticity on the outboard blade sections and an additional correction is required.

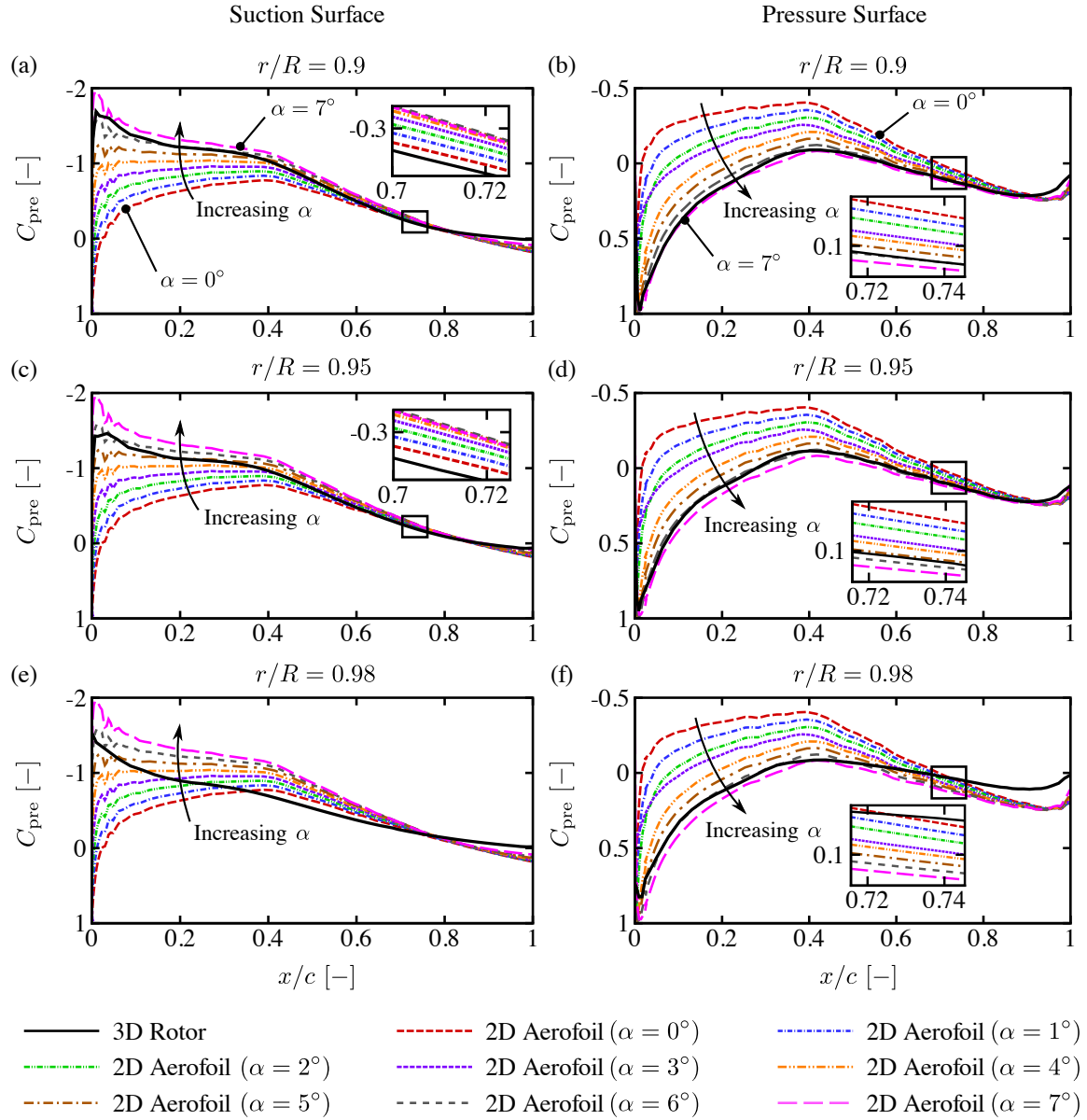


Figure 7. Static pressure distribution on three slices through the MEXICO rotor blade, normal to the blade axis. The 2D static pressure distributions were taken from a series of 2D computations of the NACA 64-418 aerofoil.

Fig. 8 shows the static pressure coefficient distribution on three slices through the Tidal rotor blade (normal to the blade axis), at $r/R = 0.9, 0.95$ and 0.98 . In these plots, the static pressure coefficient distribution for the 2D RISØ-A1-24 aerofoil is also shown for comparison, over a range of angles of attack. The changes in the static pressure coefficient distribution for the Tidal rotor show the same qualitative trends as the MEXICO rotor in Fig. 8, when moving outboard towards the tip of the blade. More specifically, at $r/R = 0.9$ the static pressure coefficient distribution near the leading edge approximately follows the 2D static pressure coefficient distribution at an angle of attack of 3° . It may be noted that this angle of attack is too low for the Tidal rotor to be operating at its design condition, as the RISØ-A1-24 aerofoil achieves its maximum lift-to-drag ratio at an angle of attack of around $6 - 7^\circ$ [17]. This is because, although the Tidal rotor is operating at its design tip-speed-ratio, the Tidal rotor is designed to operate in close proximity to other devices (high blockage) and all the computations in this work were carried out in a virtually unblocked domain. The interaction effects between neighbouring devices will be investigated in a separate study, as the fundamental characteristics of the tip loss mechanism are also likely to be affected by device proximity.

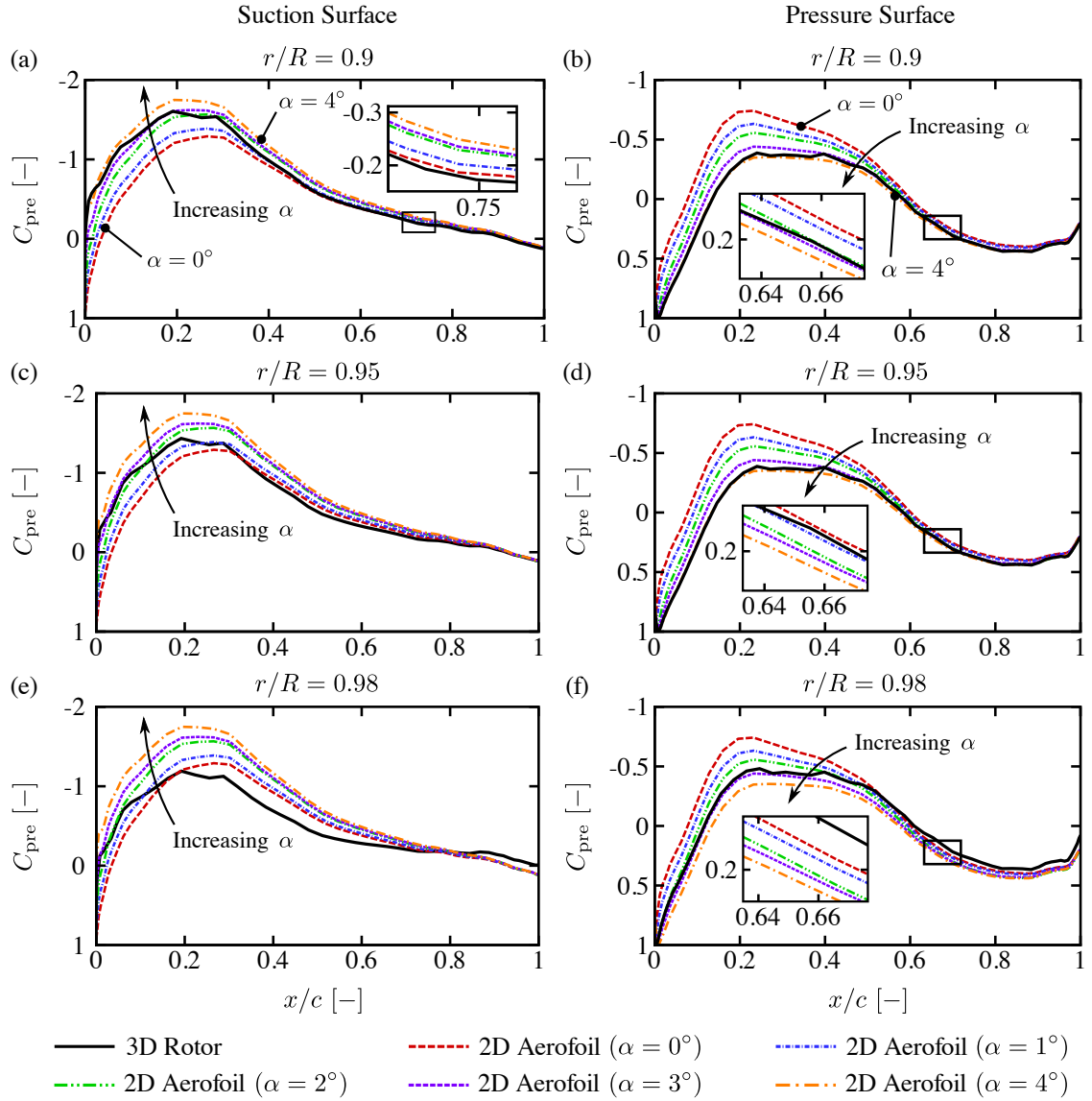


Figure 8. Static pressure distribution on three slices through the Tidal rotor blade, normal to the blade axis. The 2D static pressure distributions were taken from a series of 2D computations of the RISQ-A1-24 aerofoil.

Moving outboard to $r/R = 0.95$, the static pressure coefficient distribution near the leading edge now more closely follows the 2D static pressure coefficient distribution at an angle of attack of somewhere between 2° and 3° . Continuing outboard to $r/R = 0.98$, the static pressure coefficient distribution near the leading edge now follows the 2D static pressure coefficient distribution at an angle of attack of somewhere between 0° and 2° . As the twist angle of the aerofoil sections is constant between $r/R = 0.9$ and $r/R = 0.98$ (see Fig. 1 (b)), the angle of the incident flow vector to the rotor plane (ϕ) therefore appears to reduce by up to 3° when moving outboard from $r/R = 0.9$ to $r/R = 0.98$ on the Tidal rotor.

Moving along the chord towards the trailing edge, the static pressure distribution on both the pressure and suction surfaces of the Tidal rotor blade starts to depart from the 2D static pressure distributions, in a similar manner to the MEXICO rotor blade. On the suction surface, the static pressure increases over the majority of the aerofoil surface ($x/c < 0.8$) and reduces slightly near the trailing edge ($x/c > 0.8$). Conversely, the static pressure on the pressure surface remains relatively unchanged over the leading half of the aerofoil surface ($x/c < 0.4$) and starts to decrease over the rear half of the aerofoil surface ($x/c > 0.4$). These static pressure changes follow directly from the spanwise flow acceleration on the pressure surface and spanwise flow deceleration on the suction surface, which can be seen in Fig. 4.

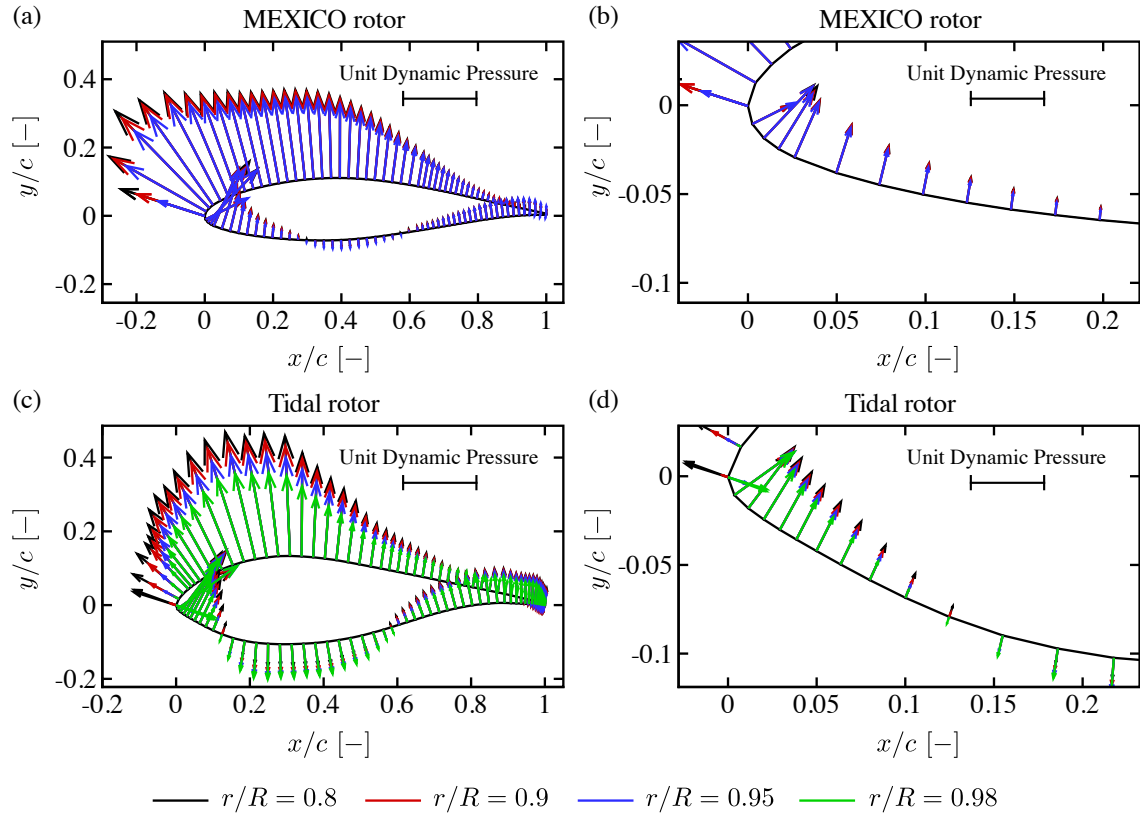


Figure 9. Vector plots of the static pressure coefficient distribution on slices through the MEXICO rotor blade (a and b) and the Tidal rotor blade (c and d), normal to the blade axis. Close-up views of the leading edge are shown in (b) and (d). The vectors are scaled by unit incident dynamic pressure, $\frac{1}{2}\rho(U_\infty^2 + (r\Omega)^2)$. The vectors at $r/R = 0.98$ are not shown for the MEXICO rotor, as this region is part of the tapered tip geometry.

6. SECTIONAL BLADE LOADING

In order to identify the consequences of the changing static pressure distribution on the sectional blade loading, Fig. 9 shows vector plots of the static pressure coefficient vector (the static pressure coefficient multiplied by the unit normal vector) for the MEXICO rotor and the Tidal rotor. In these plots, vectors pointing out of the surface indicate a negative static pressure coefficient (suction), while vectors pointing into the surface indicate a positive static pressure coefficient (positive pressure). The x and y axes are aligned parallel and perpendicular to the local chord line (respectively) and the pitch angle of the outboard blade sections of both rotors is relatively small (between 0.3° and 2.7°). Hence, the $-x$ and $+y$ axes approximately correspond with the torque and thrust producing directions (respectively).

To accompany these plots, Fig. 10 shows vector plots of the difference in static pressure coefficient vector between each radial station and an inboard radial station ($r/R = 0.8$) where the induction from the shed vorticity is small. The components of these vectors that are parallel and perpendicular to the local chordline are also shown in Fig. 10, to help identify the regions of the aerofoil surface that contribute to the changes in the sectional thrust and torque producing forces. Fig. 10 shows that both the thrust and torque producing forces drop off as the tip of the blade is approached (an increase in positive x direction force is a reduction torque, while an increase in negative y direction force is a reduction in thrust). While the sectional torque reduction is highly localised to the region around the leading edge of the suction surface, the sectional thrust reduction is more evenly distributed over the entire aerofoil surface, with contributions from both the pressure and suction surfaces.

To quantitatively observe the effect of the changing static pressure distribution on the sectional blade loading, Fig. 11 shows the cumulative integral (in the chordwise direction) of the incremental thrust and torque producing forces acting on each aerofoil section. These incremental forces were computed on a cell by cell basis by summing the surface pressure and wall shear force vectors and then resolving the resultant vector in the thrust and torque producing directions. At $r/R = 0.8$, 279.6 N/m (83%) of the total thrust producing force per unit span (334.9 N/m) on the MEXICO rotor blade is generated by the suction surface. This contribution is distributed over the entire suction surface and is stronger near the leading edge

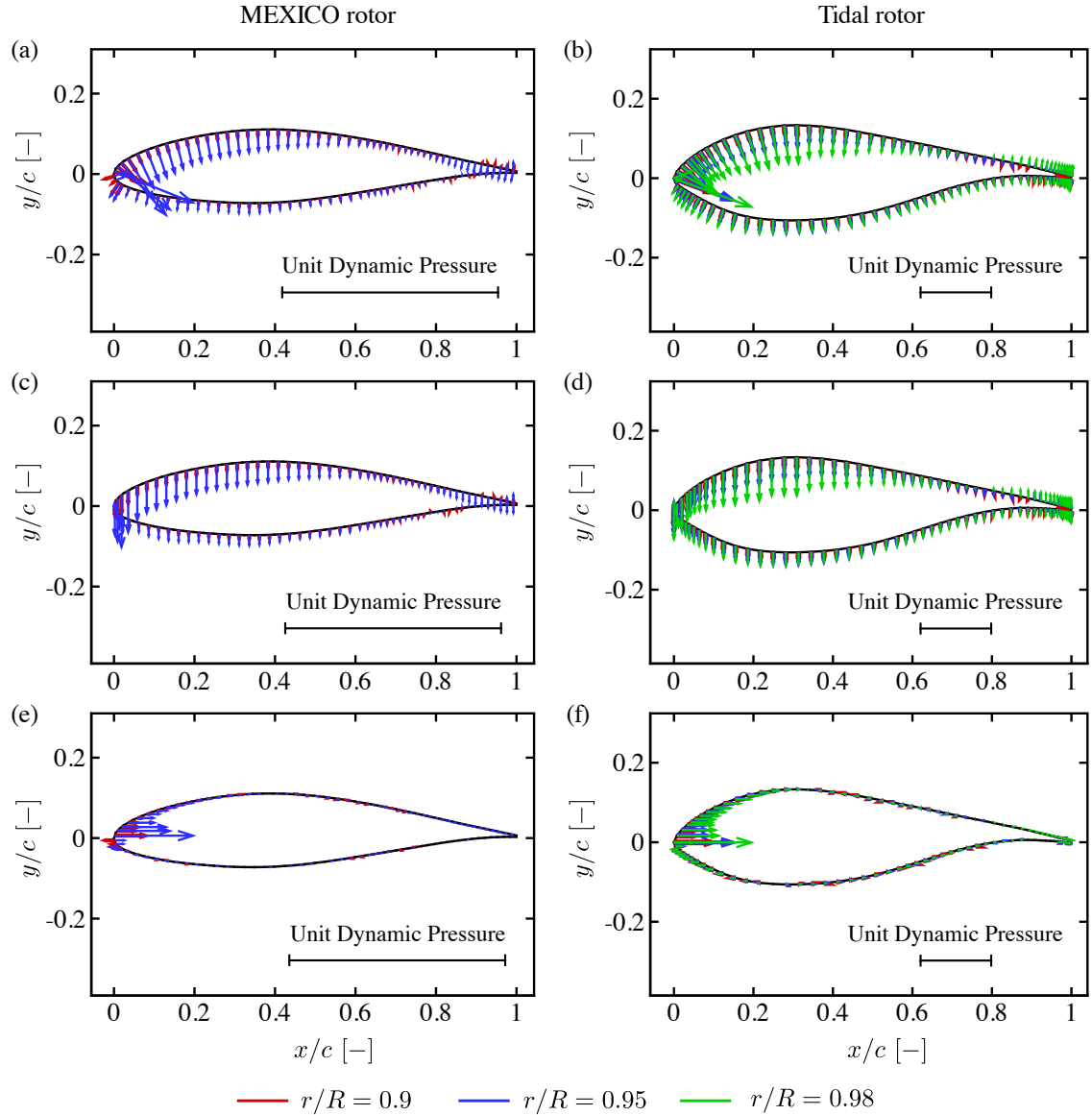


Figure 10. Vector plots of the difference in static pressure coefficient vector between each radial station and the inboard radial station at $r/R = 0.8$. The complete vector is shown in (a) and (b), the component normal to the chordline is shown in (c) and (d) and the component parallel with the chordline is shown in (e) and (f). The vectors are scaled by unit incident dynamic pressure, $\frac{1}{2}\rho(U_\infty^2 + (r\Omega)^2)$. The vectors at $r/R = 0.98$ are not shown for the MEXICO rotor, as this region is part of the tapered tip geometry.

(due to the blade suction peak). The regions near the leading and trailing edges of the pressure surface also give a positive contribution to the thrust producing force per unit span (as indicated by the increasing cumulative integral). However, their contribution to the thrust producing force per unit span (28.1 N/m for $x/c < 0.1$ and 21.6 N/m for $x/c > 0.6$) is much smaller than the contribution provided by the suction surface.

The torque producing force per unit span is more concentrated than the thrust producing force per unit span, with 56.6 N/m (out of a net total of 36.4 N/m) of torque producing force per unit span being generated over the leading 25% of the suction surface of the MEXICO rotor blade at $r/R = 0.8$. A small positive contribution to the torque producing force per unit span is also generated near the trailing edge of the pressure surface (2.2 N/m from $0.6 < x/c < 1.0$). However, over the remainder of the pressure and suction surfaces, the surface pressure distribution provides a negative contribution to the torque producing force (as indicated by the decreasing cumulative integral).

The relative spanwise reduction in the sectional thrust and torque producing forces can be computed from Fig. 11, by comparing the cumulative integrals on the inboard ($r/R = 0.8$) and outboard ($r/R = 0.95$) stations. For both rotors,

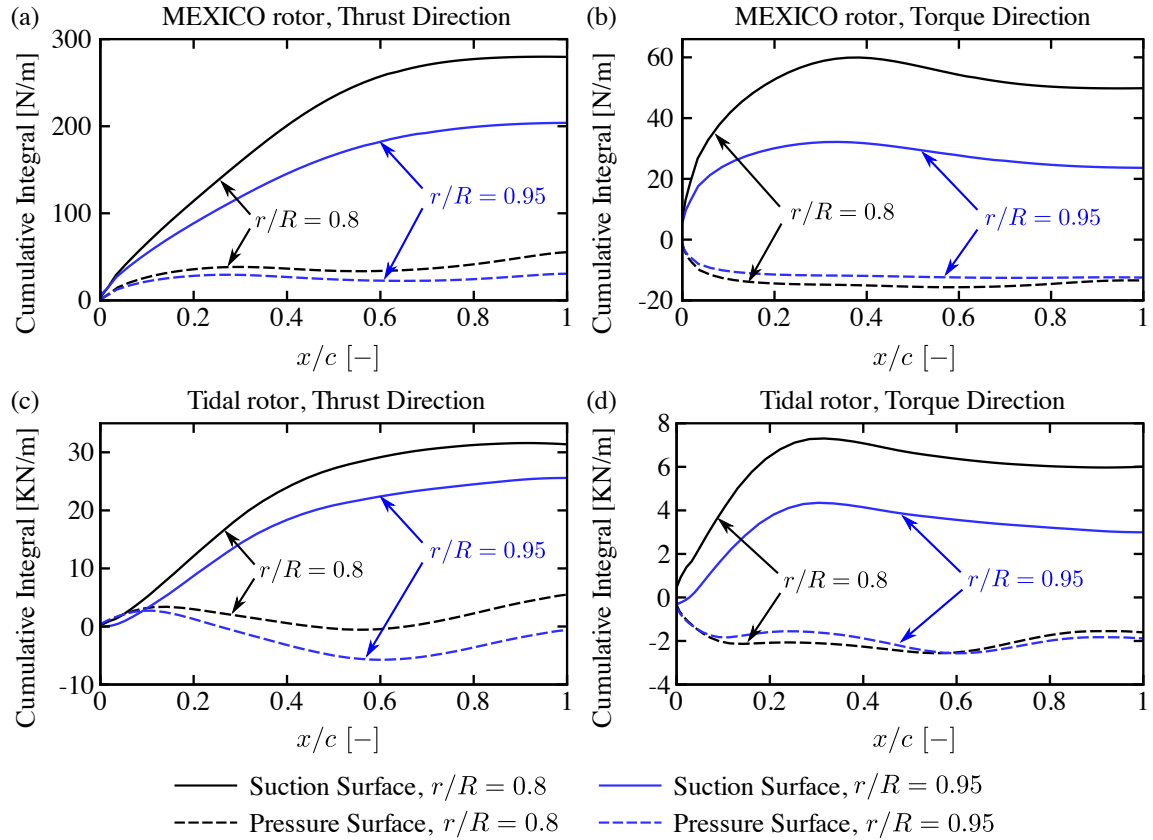


Figure 11. Cumulative integral in the chordwise direction of the incremental thrust and torque producing forces on a slice through the MEXICO rotor blade and the Tidal rotor blade (normal to the blade axes), at $r/R = 0.8$ and $r/R = 0.95$.

the relative reduction in torque producing force (69% for the MEXICO rotor and 76% for the Tidal rotor) is larger than the relative reduction in thrust producing force (30% for the MEXICO rotor and 33% for the Tidal rotor), when moving outboard from $r/R = 0.8$ to $r/R = 0.95$. Furthermore, the majority of this reduction in torque producing force can be attributed to the suction surface, as the cumulative integral of the torque producing force on the pressure surface remains relatively unchanged when moving outboard from $r/R = 0.8$ to $r/R = 0.95$. The implications of these observations will be discussed in more detail in the next section.

7. FORCE VECTOR ROTATION

The static pressure distributions in Fig. 9, together with the wall shear stress distributions, were integrated in the chordwise direction to compute the total sectional force vector (\mathbf{F}) acting on each of the outboard blade sections. The total sectional force vectors are shown in Fig. 12 and have been placed at the calculated centre of pressure of their respective aerofoil sections. To aid with the interpretation of Fig. 12, Table I shows the magnitude of the total sectional force vector ($|\mathbf{F}|$), the angle of the sectional force vector relative to the rotor plane (θ) and the chordwise location of the centre of pressure (x_p).

Fig. 12 shows that (for both rotors) the sectional force vector reduces in magnitude and rotates (in a clockwise sense) towards the streamwise direction as the tip of the blade is approached. These changes follow directly from the changing shape of the static pressure distribution in Fig. 10. More specifically, since the strength of the suction developed on the suction surface and the pressure developed on the pressure surface both reduce as the tip of the blade is approached (due to inboard and outboard spanwise momentum transport respectively), the sectional force vector must reduce in magnitude. Additionally, the large reduction in suction generated near the leading edge of the suction surface of the aerofoil leads to the torque producing force dropping off more rapidly than the thrust producing force, which causes the sectional force vector to rotate (in a clockwise sense) towards the streamwise direction.

Fig. 12 also shows that, as another consequence of the changing static pressure distribution, the centre of pressure moves in the chordwise direction (towards the trailing edge) as the tip of the blade is approached. However, the magnitude

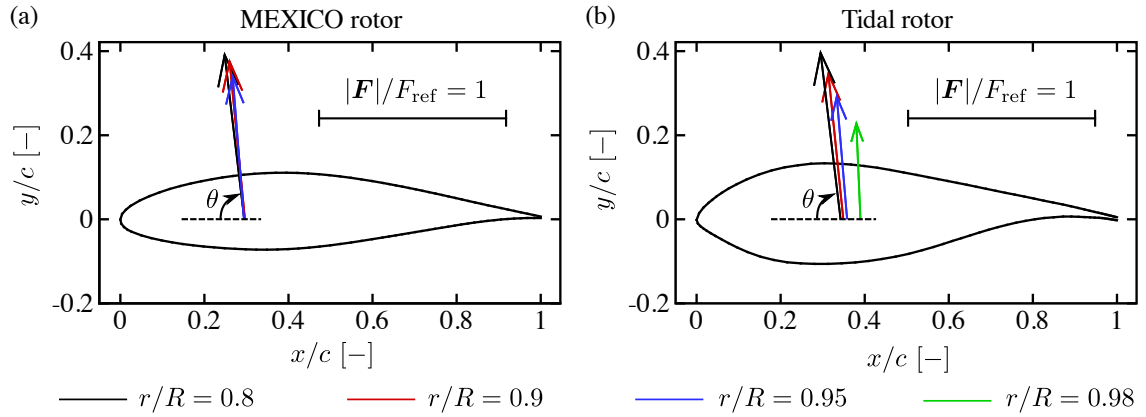


Figure 12. Vector plots of the sectional force vector acting on selected outboard sections of the MEXICO rotor blade and the Tidal rotor blade. The vectors have been placed with their origin at the centre of pressure (along the line $y/c = 0$) of their respective aerofoil sections. Here θ represents the angle of the sectional force vector to the chord line. The vectors are scaled on the reference force $F_{\text{ref}} = \frac{1}{2} \rho (U_{\infty}^2 + (r\Omega)^2) c$. The vector at $r/R = 0.98$ is not shown for the MEXICO rotor, as this region is part of the tapered tip geometry.

Table I. Magnitude of the total sectional force vector ($|F|$), angle of the total sectional force vector relative to the rotor plane (θ) and the chordwise position of the centre of pressure (x_p). The reference sectional force $F_{\text{ref}} = \frac{1}{2} \rho (U_{\infty}^2 + (r\Omega)^2) c$. The tabulated values at $r/R = 0.98$ are not shown for the MEXICO rotor, as this region is part of the tapered tip geometry.

Rotor	r/R [-]	$ F /F_{\text{ref}}$ [-]	θ [$^{\circ}$]	x_p/c [-]
MEXICO rotor	0.8	0.876	84.0	0.295
MEXICO rotor	0.9	0.838	85.1	0.296
MEXICO rotor	0.95	0.757	86.1	0.294
Tidal rotor	0.8	0.887	83.1	0.343
Tidal rotor	0.9	0.774	84.2	0.349
Tidal rotor	0.95	0.651	85.2	0.358
Tidal rotor	0.98	0.507	87.5	0.390

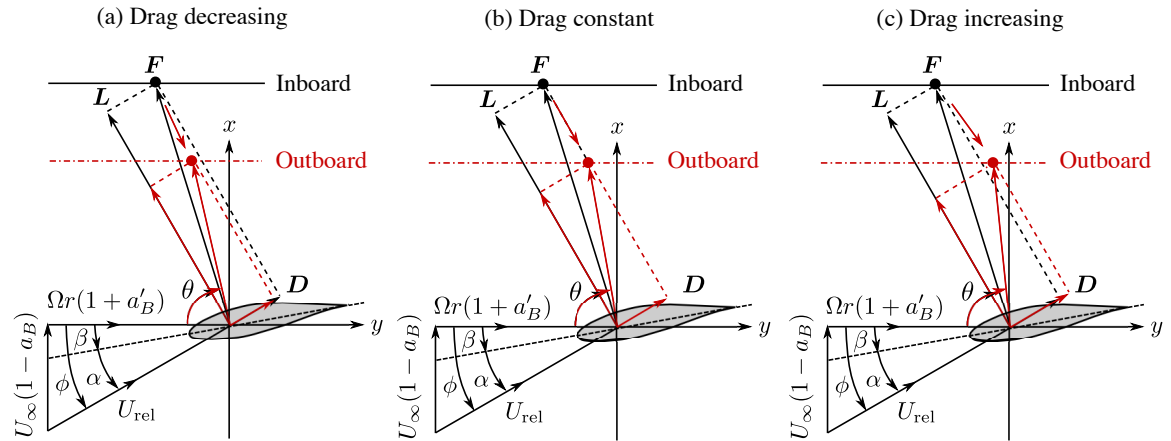


Figure 13. Blade element diagram for an inboard section of the rotor blade (black lines) where the induction from the shed vorticity is negligible and an outboard section of the rotor blade (red lines) where the induction from the shed vorticity is significant. The sectional drag force per unit span may (a) decrease, (b) remain constant or (c) increase, depending on the degree of rotation of the total sectional force vector (F).

of this movement is small for both rotors (less than 1.5% of the chord length between $r/R = 0.8$ and 0.95) and is therefore unlikely to be of primary importance in the subsequent analysis of these rotors and is neglected here.

The reduction in magnitude and rotation of the sectional force vector can be used to explain many observations of the blade loading distribution that have been made in the literature. To facilitate the following explanation, Fig. 13 shows a blade element diagram to represent the vector components of the total sectional force vector that are exerted on an inboard section and an outboard section of the rotor blade. Here the inboard section represents a section far from the blade tip (say $r/R = 0.8$) where the induction from the shed vorticity (both downwash and spanwise flow along the blade) is negligible, while the outboard section represents a section near the tip of the blade (say $r/R = 0.95$) where the induction from the shed vorticity is more significant.

There are three possible scenarios that are consistent with the observed variation of the blade loading on the outboard sections of the rotor. They are all shown in Fig. 13. In order for the total sectional force vector to reduce in magnitude and rotate towards the streamwise direction, the sectional lift force per unit span (L) must reduce. However, the sectional drag force per unit span (D) may decrease, remain constant, or increase, resulting in different degrees of rotation. While all three scenarios are permissible and consistent with the observed behaviour of the sectional force vector (clockwise rotation), the degree of rotation (and therefore the behaviour of the sectional drag coefficient) is not known at this stage of the analysis. Hence, it is not possible to strictly classify the behaviour of the drag coefficient on the outboard sections of all rotors as either Fig. 13 (a), (b) or (c), since all three scenarios are permissible with a clockwise rotation and a reduction in magnitude of the sectional force vector. However, (by carrying out additional analyses) the majority of rotors investigated in the literature have shown an increase in the sectional drag coefficient on the outboard blade sections (see Johansen and Sorenson [23] and Shen et al. [24] for example). This was also found to be the case for the MEXICO rotor by Wimshurst and Willden [10]. Hence, the rotation of the sectional force vector corresponds with Fig. 13 (c) for these rotors.

Fig. 13 can also be used to better understand and classify different tip flow correction methods. For example, tip flow corrections that only reduce the angle of attack (such as Prandtl [5] type corrections), reduce both the lift and drag coefficients as the tip of the blade is approached (assuming of course that the aerofoil is not stalled and $\alpha > 0$). As the drag coefficient is reduced, these correction methods implicitly assume that the reduction in magnitude and rotation of the sectional force vector corresponds with Fig. 13 (a), provided that the lift coefficient reduces faster than the drag coefficient (which is the case for most aerofoils). Hence, these methods will be insufficient for correcting the blade loading if the rotation of the sectional force vector (for a given rotor that is to be corrected) is observed to be greater, along the lines of Fig. 13 (b) or (c). In a similar manner, tip flow correction methods that only reduce the lift coefficient or the circulation strength implicitly assume that the rotation of the sectional force vector corresponds with Fig. 13 (b), as the drag coefficient is not corrected by these methods. Hence, these methods will also be insufficient for correcting the blade loading if the rotation of the sectional force vector (for a given rotor that is to be corrected) is observed to be greater, along the lines of Fig. 13 (c). It follows that blade loading based corrections i.e. those directly correcting the thrust and torque distributions, must be anisotropic in order to cover the range of permissible rotations shown in Fig. 13. For example, Wimshurst and Willden's [10, 25] anisotropic extension of the original isotropic model of Shen et al. [9] is one approach that could be taken to correct the blade loading.

8. CONCLUSIONS

At the tip of a 3D rotor blade, the flow is driven from the pressure surface around the tip to the suction surface, by the static pressure difference that is apparent between the surfaces. This rotational flow component is convected downstream into the rotor wake as shed vorticity. The shed vorticity induces a downwash at the rotor plane and spanwise flow accelerations along the blade. While the induced downwash leads to a reduction in angle of attack at the rotor plane, the spanwise flow accelerations lead to additional momentum transport along the blade surfaces. With these changes to the local flow field, the surface pressure distribution can no longer be accurately approximated by the pressure distribution experienced by the same aerofoil section under 2D flow conditions. As the tip of the blade is approached, the induction from the shed vorticity increases and the static pressure distribution departs further from 2D flow conditions. It follows that a correction to the angle of attack alone will always be insufficient to correct the blade loading computed by low order rotor models that are based on sectional aerofoil data (such as the blade element momentum method).

In this paper, the static pressure changes that arise from the shed vorticity on the outboard sections have been examined. It has been shown that (in general) the static pressure on the suction surface increases and the static pressure on the pressure surface reduces as the tip of the blade is approached. This results in the magnitude of the sectional force vector reducing as the tip of the blade is approached. In addition, a large reduction in the suction developed near the leading edge of the suction surface causes the torque producing force to drop off more rapidly than the thrust producing force. As a result, the sectional force vector rotates (in a clockwise sense) towards the streamwise direction as the tip of the blade is approached. The anisotropic reduction in the thrust and torque distributions gives good agreement with observations of other rotors carried out in the literature and must be accounted for by tip flow corrections if the blade loading is to be computed with sufficient accuracy.

ACKNOWLEDGEMENT

The authors would like to thank EPSRC and Uniper Technologies Ltd. for funding the CASE-Studentship for this project and the Advanced Research Computing facility at the University of Oxford where the computations were performed. The authors would also like to thank the consortium that carried out the EU FP5 project MEXICO. They provided a computer-aided design file containing the geometry of the MEXICO rotor blade that was used to generate the blade resolved mesh.

REFERENCES

1. Hansen M, Johansen J. Tip studies using CFD and comparison with tip loss models. *Wind Energy* 2004; **7**:343–356.
2. Madsen H, Fuglsang P. Numerical investigation of different tip shapes for wind turbine blades. *Technical Report Risø-R-891(EN)*, Risø National Laboratory, Roskilde, Denmark 1996.
3. Ferrer E, Munduate X. Wind turbine blade tip computations using CFD. *Journal of Physics: Conference Series* 2007; **75**:012 005.
4. Johansen J, Sørensen N. Aerodynamic investigation of winglets on wind turbine blades using CFD. *Technical Report Risø-R-1543(EN)*, Risø National Laboratory, Roskilde, Denmark 2006.
5. Betz A. Schraubenpropeller mit geringstem Energieverlust. Mit einem Zusatz von L. Prandtl. *Nachrichten von der Gesellschaft der Wissenschaften zu Göttingen, Mathematisch-Physikalische Klasse* 1919; :193–217.
6. Goldstein S. On the vortex theory of screw propellers. *Proc. R. Soc. A* 1929; **123**(792):440–465.
7. Glauert H. Airplane propellers. *Aerodynamic Theory*, Julius Springer: Berlin, 1935; 169–360.
8. Burton T, Jenkins N, Sharpe D, Bossanyi E. *Wind Energy Handbook*. John Wiley & Sons Ltd.: West Sussex, UK, 2011.
9. Shen W, Mikkelsen R, Sørensen J, Bak C. Tip loss corrections for wind turbine computations. *Wind Energy* 2005; **8**:457–475.
10. Wimshurst A, Willden RHJ. Analysis of a tip correction for horizontal axis turbines. *Wind Energy* 2017; **20**(9):1515–1528, doi:10.1002/we.2106. URL <http://dx.doi.org/10.1002/we.2106>.
11. Schepers JG, Boorsma K, Cho T, Gomez-Iradi S, Schaffarczyk P, Jeromin A, Shen WZ, Lutz T, Meister K, Stoevesandt B, *et al.*. Final report of IEA task 29, Mexnext (phase 1): Analysis of MEXICO wind tunnel measurements. *Technical Report ECN-E12-004*, Energy Research Centre of the Netherlands (ECN) February 2012.
12. Boorsma K, Schepers JG. Description of experimental setup, MEXICO measurements. *Technical Report ECN-X-09-0XX*, Energy Research Centre of the Netherlands (ECN) 2009.
13. Bechmann A, Sørensen N, Zahle F. CFD simulations of the MEXICO rotor. *Wind Energy* 2011; **14**:677–689.
14. Guntur S, Sørensen N. A study of rotational augmentation using CFD analysis of flow in the inboard region of the MEXICO rotor blades. *Wind Energy* 2015; **18**:745–756.
15. Wimshurst A, Willden RHJ. Extracting lift and drag polars from blade resolved computational fluid dynamics for use in actuator line modelling of horizontal axis turbines. *Wind Energy* 2017; **20**(5):815–833, doi:10.1002/we.2065. URL <http://dx.doi.org/10.1002/we.2065>.
16. Schluntz J, Willden RHJ. The effect of blockage on tidal turbine rotor design and performance. *Renewable Energy* 2015; **81**:432–441.
17. Wimshurst A, Willden RHJ. Computational analysis of blockage designed tidal turbine rotors. *Proceedings of the 2nd International Conference on Renewable Energies Offshore (RENEW 2016)*, Lisbon, Portugal, 2016; 587–597.
18. Plaza B, Bardera R, Visiedo S. Comparison of BEM and CFD results for MEXICO rotor aerodynamics. *Journal of Wind Engineering and Industrial Aerodynamics* 2015; **145**:115–122.
19. Menter FR. Two-equation eddy-viscosity turbulence models for engineering applications. *AIAA Journal* 1994; **32**(8):1598–1605.
20. Patankar SV. *Numerical Heat Transfer and Fluid Flow*. Hemisphere Publishing Corporation: Washington DC USA, 1980.
21. Sweby PK. High resolution schemes using flux limiters for hyperbolic conservation laws. *SIAM Journal on Numerical Analysis* 1984; **21**:995–1011.
22. Gant S, Stallard T. Modelling a tidal turbine in unsteady flow. *International Offshore and Polar Engineering Conference*, Vancouver, Canada, 2008; 473–479.
23. Johansen J, Sørensen NN. Aerofoil characteristics from 3D CFD rotor computations. *Wind Energy* 2004; **7**:283–294.
24. Shen W, Hansen M, Sørensen J. Determination of the angle of attack on rotor blades. *Wind Energy* 2009; **12**:91–98.
25. Wimshurst A, Willden RHJ. Spanwise flow corrections for tidal turbines. *12th European Wave and Tidal Energy Conference (EWTEC 2017)*, Cork, Ireland, 2017.